SOLID-STATE PHYSICS

Full momentum- and energy-resolved spectral function of a 2D electronic system

Joonho Jang,[1]* Heun Mo Yoo,[1] L. N. Pfeiffer,[2] K. W. West,[2] K. W. Baldwin,[2] Raymond C. Ashoori[1]*

The single-particle spectral function measures the density of electronic states in a material as a function of both momentum and energy, providing central insights into strongly correlated electron phenomena. Here we demonstrate a high-resolution method for measuring the full momentum- and energy-resolved electronic spectral function of a two-dimensional (2D) electronic system embedded in a semiconductor. The technique remains operational in the presence of large externally applied magnetic fields and functions even for electronic systems with zero electrical conductivity or with zero electron density. Using the technique on a prototypical 2D system, a GaAs quantum well, we uncover signatures of many-body effects involving electron-phonon interactions, plasmons, polarons, and a phonon analog of the vacuum Rabi splitting in atomic systems.

Inside of semiconductors and metals, negatively charged electrons interact with each other and with positively charged ions and impurities, creating complex many-particle systems (*1*). Despite the strong electron-electron Coulomb repulsions in solids, Landau-Fermi liquid theory predicts that in a degenerate Fermi system, electrons near the Fermi energy level E_F behave as weakly interacting quasiparticles (*1*, *2*). This happens because the degenerate electrons below the Fermi level screen the Coulomb potential between particles and restrict the phase space available for excited electrons to scatter. When energies of electron interactions are large compared with the Fermi energy, such as for systems with low electron density and/or under strong magnetic fields, the description in terms of weakly interacting quasiparticles of the Fermi liquid theory no longer applies; electrons show strongly correlated behaviors, accompanied by unscreened, effectively enhanced electron-phonon (e-ph) and electron-electron (e-e) interactions. This phenomenon affects experimentally important quantities—e.g., transport, thermodynamic, and optical properties—and may lead to exotic phases such as superconductivity and the fractional quantum Hall effect (*3*, *4*).

The spectral function—the distribution of single-particle electronic states in energy and momentum space—is a fundamental physical quantity that directly reflects underlying many-body interactions. Physicists have extensively developed the theory of the spectral function of electron liquid and strongly correlated electron systems (*1*, *2*, *5*, *6*). Established tools such as scanning tunneling microscopy and angle-resolved photoemission spectroscopy (ARPES) have contributed greatly to the understanding of the electronic structure of solids by measuring the spectral function or quantities related to it (*7*, *8*). However, these methods only probe the electronic systems at the sample surface and do not work if the sample is electrically insulating. Thus, there has been no means for accurate determination of the spectral function of subsurface electronic systems created by molecular beam epitaxy (MBE), such as GaAs/GaAlAs quantum wells (QWs), a long-time testbed for understanding fundamental physics (e.g., quantum Hall effects) and device applications. Most experimental studies in these systems use transport or thermodynamic probes that have sensitivity only to the average thermodynamic behavior of electrons near the Fermi energy.

Here we demonstrate a method of tunneling spectroscopy, termed momentum- and energy-resolved tunneling spectroscopy (MERTS), that utilizes fine control of the momentum and energy of tunnel-injected electrons and directly measures the spectral functions of a 2D electron system in a QW at various densities, including near-depleted and fully depleted (insulating) regimes. This technique can visualize the pronounced e-ph and e-e interaction effects deep inside solids.

In MERTS, we controllably generate a collimated packet of electrons with precisely defined energy E and momentum k from an adjacent probe layer (a 2D QW) and, by means of tunneling, inject the electrons into the unoccupied quantum states of the target 2D system to measure its spectral function. Electrons from this collimated beam can tunnel into the target 2D electron system only when unoccupied states are available with the same energy and momentum, resulting in E-k selectivity of the tunneling process (Fig. 1). The tunneling probability is, as a result, directly proportional to the spectral function for adding a particle into the 2D system (*1*, *2*, *9*). To achieve high E-k resolution, in the probe layer, we prepare electrons with a very small Fermi surface (containing a very low density of electrons $n \approx 3 \times 10^{10}$ cm^{-2}, with $E_F \approx 1.0$ meV and $k_F \approx 0.004$ Å^{-1}; these numbers set the resolution of the technique) at $E = 0$ and $k = 0$ (Γ-point in the GaAs conduction band minimum), and we translate the momentum of the packet by using a magnetic field $B_{||}$ applied perpendicular to the tunneling direction, giving electrons a momentum shift of $\Delta k_{x,y} = eB_{\parallel y,x}d_t/\hbar$ in the tunneling process (*10*, *11*). Here, $\Delta k_{x,y}$ is the momentum translation of the tunneling electrons, e is the electron charge, d_t is the tunneling distance, and $\hbar$ is the reduced Planck constant (Fig. 1, B and C). This effect can be understood semiclassically as the momentum gain of an electron in traversing the tunnel barrier caused by the magnetic field–induced Lorentz force. Investigators have previously used such momentum boosts for examining band dispersions in magnetotunneling studies of 2D systems (*10*–*13*), quantum dots (*14*), and single donors (*15*). For 2D systems (*10*–*13*), the measurements in these works involved large Fermi surfaces in both the probe and target wells, resulting in tunneling currents that reflect convolutions of two systems and variations in the in-plane electrical conductivity in both layers, making it unfeasible to obtain detailed spectral information. In contrast, in MERTS, we achieve full momentum and energy resolution by adapting a pulsed tunneling method (*16*) that requires no direct electrical contact to the system of two QWs and does not rely on conductivity of the 2D systems; the method functions even if either or both of the 2D systems are electrically insulating. Essential elements for effective implementation of MERTS include (i) maintenance of a small (pointlike) Fermi surface of source electrons (probe layer); (ii) elimination of lateral transport in either layer, ensuring uniform tunneling at all points in the plane; (iii) full tunability of the density in the target layer; and (iv) a short-duty cycle pulsed technique that ensures probing of a cold electronic state of the target system.

An example of tunneling spectra of a 2D electron system in a GaAs/AlGaAs QW (Fig. 1A), measured with $B_{||}$ applied along [100] (x axis) and [010] (y axis), is plotted in Fig. 1E. We verified the high fidelity of the momentum and energy conservation in the tunneling process by comparison to a numerical simulation performed with the same parameters (fig. S3). The MBE-grown wafer is specifically designed so that the probe well has the low density described above. The probe and target layers exist in a two-terminal capacitor structure (Fig. 1A). We vary the density of the target 2D system by applying a dc voltage V_b across the top and bottom electrodes, drawing charges from the top capacitor electrode into the target layer. In addition to V_b, we apply repetitive short-duration (~100-ns) voltage pulses to induce the tunneling voltage $V_t = E_t/e = (E - E_F)/e$ between the source and target layer. Each voltage pulse induces electrons to tunnel (vertically as in Fig. 1A) from the probe layer into the target layer. This vertical movement of charge results in the accumulation of image charges on the top electrode

[1]Department of Physics, Massachusetts Institute of Technology (MIT), Cambridge, MA 02139, USA. [2]Department of Electrical Engineering, Princeton University, Princeton, NJ 08544, USA. *Corresponding author. Email: jjang7@mit.edu (J.J.); ashoori@mit.edu (R.C.A.)

of the capacitor, which we detect using a high-electron-mobility transistor amplifier. Taking the time derivative of this signal yields the tunneling current. Between the short pulses, we apply an opposite polarity pulse with duration controlled by feedback to bring the target system back to its original charge density and include a (10- to 100-ms) time delay to provide the target system time to cool back down to a very low electron temperature (*17*). In MERTS, the electronic density of states (DOS) is directly proportional to the tunneling current I, in contrast to prior tunneling measurements using a 3D electrode in which the DOS was proportional to dI/dV (*16*).

In Fig. 2, A to C, we show the E-k distributions (dispersions) of electronic states at various carrier densities n. We calibrate the momentum axis, proportional to $B_{||}$, on the basis of our knowledge of the tunneling distance d_t determined from numerical simulations of the wave functions in each QW (designed to be d_t = 26 nm, but changing slightly with V_b). Adjusting V_b to more negative values decreases the electron density of the target QW and eventually fully depletes it. The spectrum labeled as an empty well in Fig. 2C shows the depletion of electrons from the conduction band, visualized by the bottom of the conduction band edge rising above the Fermi level. The absence of occupied extended electron states in the QW is a clear signature of a system entering an insulating phase, consistent with our capacitance measurements of the structure.

The spectra display quantized subbands owing to the confinement potential in the growth direction (z axis). We identify the three lowest subbands in the spectrum; the intensity of the spectrum is stronger for subbands lying higher in energy because the higher subband wave functions penetrate deeper into the barrier and thus have stronger tunnel coupling to the probe well. In a model of the bands that neglects e-e and e-ph interactions, the single particle energies $\varepsilon_{n,k}$ follow $\varepsilon_{n,k} = \varepsilon_{n,0} + \hbar^2/2m_{\mathrm{eff}} \times (k_x{}^2 + k_y{}^2) \times (1 + \eta|k|^2)$ (blue curves in Fig. 2E). Here, $\varepsilon_{n,0}$ is the confinement energy of the nth subband, k_x and k_y are planar momenta, m_{eff} is the band mass, and $\eta \approx -43.7$ Å^2 is a parameter that accounts for band nonparabolicity (*17*, *18*). However, a more comprehensive picture beyond this effective mass approximation comes from the description of interacting electrons with the spectral function (*1*, *2*, *7*, *9*)

$$A(E,k) = \frac{1}{\pi}\frac{|Im\Sigma|}{(E - \varepsilon_{n,k} - Re\Sigma)^2 + (Im\Sigma)^2} \quad (1)$$

where E is the energy of injected electrons in the measurement. All of the interparticle interactions that influence the electronic dispersion are summed to yield the modified complex-valued self-energy Σ of the (quasi)particles. In the quasiparticle approximation, the real part of the self-energy ($Re\Sigma$) represents the change of the particle energy, and the imaginary part ($Im\Sigma$) is proportional to the inverse of the particle lifetime (*1*, *19*). The controlled observation of this modification in the electronic dispersion would be one of the most direct ways to quantify and understand the dynamics of an interacting many-particle system.

The measured spectra in Fig. 2, A to C, at various densities display multiple features that appear to originate from many-body interactions, including the electron-to–longitudinal optical (LO) phonon coupling. Considering a LO phonon energy of 36 meV, red arrows indicate expected locations of LO phonon features at 36 meV above E_F (Fig. 2, A, B, and E), or 36 meV above the bottom of the first subband for the case of a depleted well (Fig. 2C). Blue arrows in Fig. 2, A to C and E, are placed at 36 meV above the bottom of the second subband (see also fig. S4). To corroborate the phonon effects, we modeled a self-energy Σ that includes impurity broadening and e-ph interactions in a weak-coupling limit (i.e., a perturbation theory) to calculate the simulated tunneling spectrum in Fig. 2D. The simulation involves dispersionless LO phonons interacting with electrons through the Frohlich Hamiltonian (*17*, *20*),

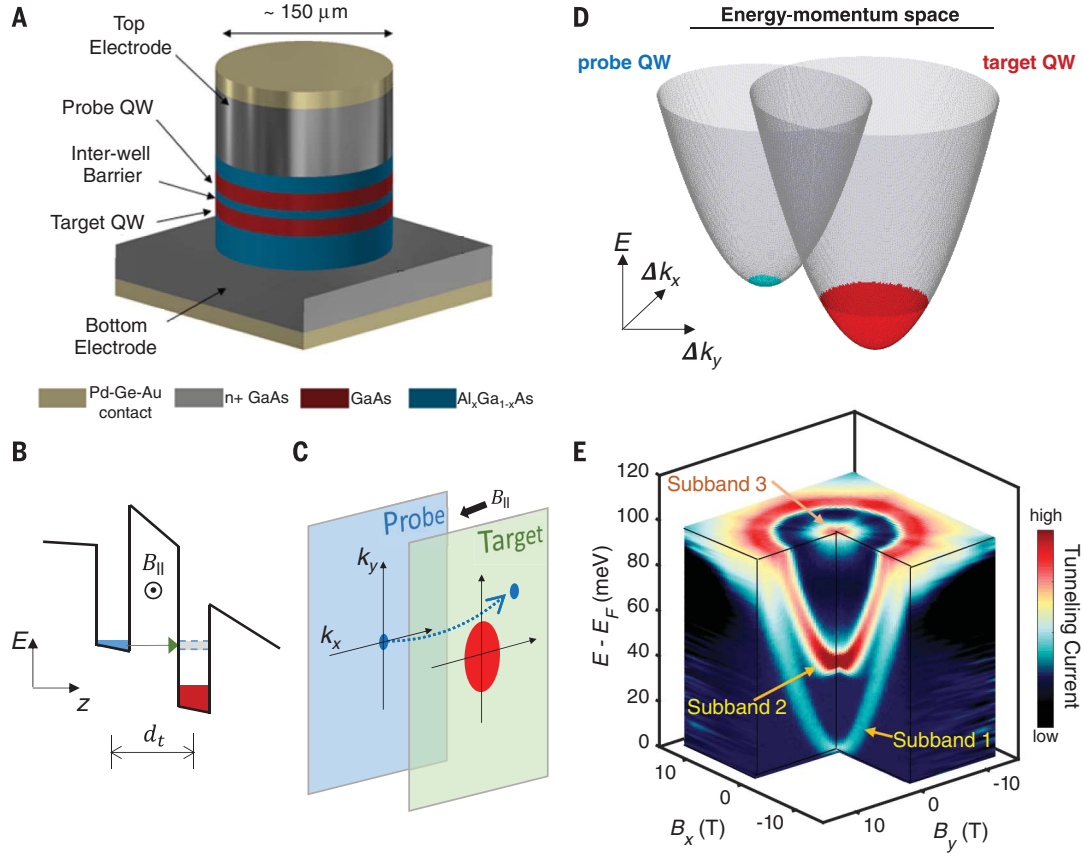

Fig. 1. Schematics of the tunneling device and principles of the energy-momentum selection process. (**A**) The vertical tunneling device used in the experiment. Two GaAs quantum wells (QWs; width of 20 nm each) are separated by an $Al_{0.8}Ga_{0.2}As$ potential barrier (6 nm). Electrons in the top (probe) QW with nearly zero planar momentum probe electronic states in the bottom (target) QW. (**B**) The injection of an electron packet probes only empty available states in the target layer. (**C**) Diagram explaining the momentum selection mechanism. The in-plane field generates a momentum boost in the tunneling process to displace the zero planar momentum into $k_{\mathrm{final}} = eB_{||}d_t/\hbar$ in the bottom QW. (**D**) E-k dispersions in the presence of the in-plane field. In (B) to (D), the occupied states are shown in blue and red for probe and target layers, respectively. (**E**) Measured spectra with $B_{||}$ along the crystallographic axis of [100] and [010] of GaAs. Multiple unoccupied QW subbands are visible.

appropriate for a polar semiconductor such as GaAs (*1*). The simulated spectrum displays key aspects of the measured spectrum, and we can identify kinks and modifications (red and blue arrows in Fig. 2D) of the spectrum generated by the e-ph coupling; comparison with measured spectra in Fig. 2, A to C and E, indicates that the features located near 36 and ~70 to 80 meV in the spectrum originate from the e-ph interaction combined with a specific subband structure.

For more quantitative analysis, we extract the real and imaginary components of the self-energy Σ by determining the peak locations and widths of momentum distribution curves (MDCs) of the spectra. We extract the self-energy using $Re\Sigma = E - \varepsilon(k_{peak})$ and $|Im\Sigma| \approx (\Delta k - 0.0032\ \text{Å}^{-1}) \times \hbar v_{g0}$ (*21*–*23*), where the subtraction of 0.0032 Å^{-1} is to take account of the finite size of the Fermi surface of the probe QW, and v_{g0} is the bare group velocity [section 5 of (*17*)]. In Fig. 2F, the extracted $Im\Sigma$ values at various densities show steplike features. These steplike features in $|Im\Sigma|$, indicated by red and blue dashed lines, correspond to the features respectively highlighted by red and blue arrows in Fig. 2, A to C and E. A steplike feature in the imaginary part of self-energy generally arises as a consequence of electrons interacting with a nearly dispersionless bosonic mode (*1*, *9*). This strongly suggests that these features in the self-energy arise from e-ph interactions in GaAs.

When the electron density of the target QW is decreased to near depletion, electrons localize in minima of a disordered potential and can no longer screen interparticle interactions. Then the validity of the perturbative calculations of the self-energy stemming from the e-ph interaction also becomes questionable [section 4 of (*17*)]. In this regime in Fig. 2C, the spectrum appears considerably different than the spectra in Fig. 2, A and B. In particular, the quasiparticle dispersion develops an unusually sharp kink emergent at an unexpected position (dashed circle). The kink structure exists only at very low density near the depletion regime and at low temperature, unlike other structures described previously. From the shape of the kink, we conjecture that a strong electron-boson coupling is emergent near electron depletion (*24*). The energy of the kink is located at $\hbar\Omega \approx 48$ meV above the first subband minimum, where $\hbar\Omega$ is the energy of the conjectured

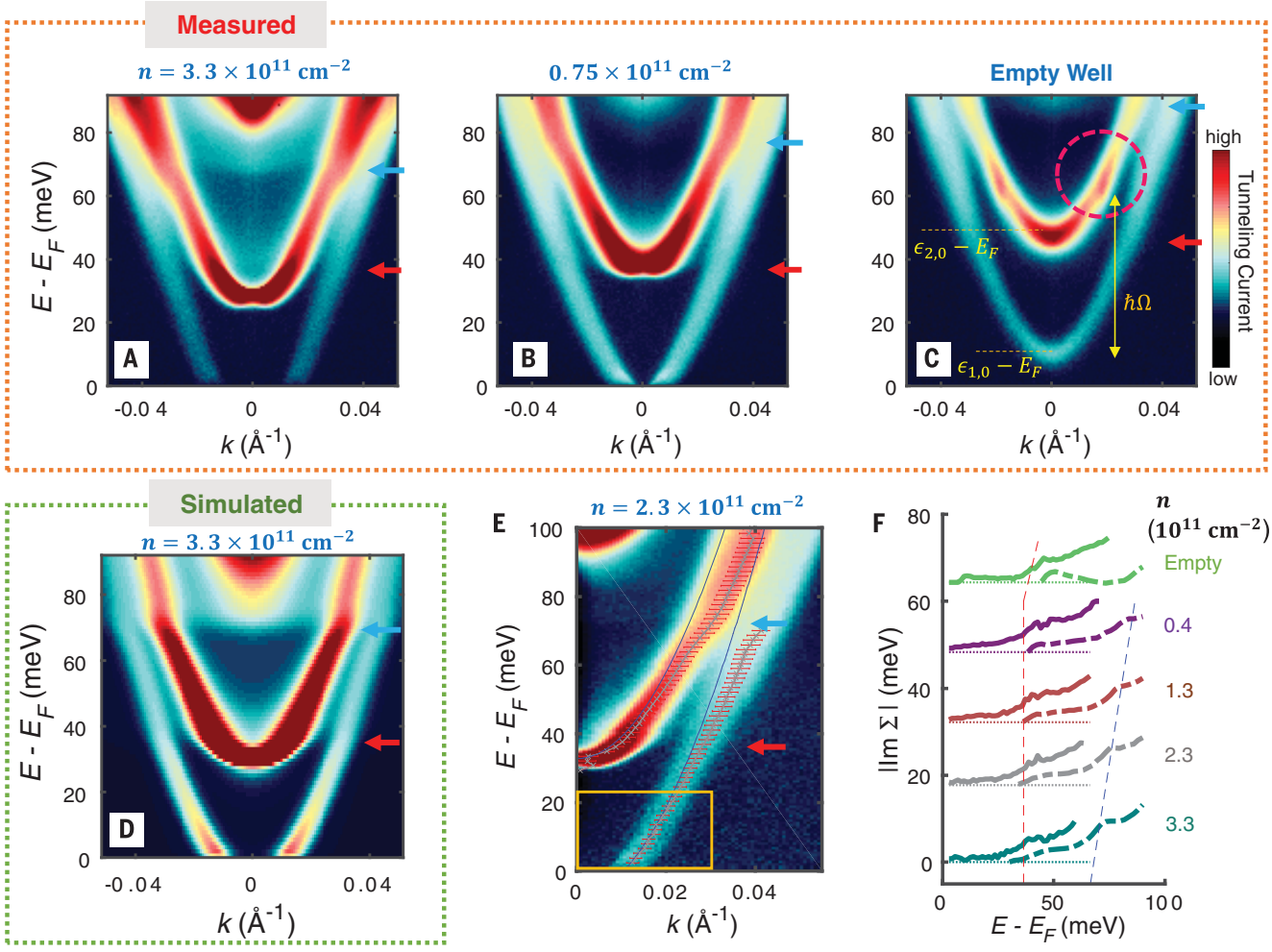

Fig. 2. MERTS spectra at various densities *n* and extraction of self-energy. (**A** to **C**) Tunneling spectra measured at 1.5 K for various target QW densities (fig. S7 shows a full data set). In (A), three subbands due to the nonzero width of the target well are visible. In (C), data are shown for a gate voltage at which the target well first fully depletes. (**D**) A tunneling spectrum simulation with a self-energy term that accounts for impurity broadening and electron-phonon interactions. (**E**) A measured *E*-*k* spectrum. The blue curves show the bare band dispersion $\varepsilon_k - E_F$ expected from detailed band structure calculations (*17*, *18*). We extract the self-energy by measuring the peak locations k_{peak} and half-widths Δk of MDCs (curves cut along the momentum axis at energy *E*). The red bars are centered at k_{peak} and have widths of Δk. The yellow box marks an area of the spectrum considered in Fig. 4. In (A) to (E), positions of red and blue arrows mark expected positions of LO phonon features. (**F**) Extracted $Im\Sigma$ values at various densities. The solid (dashed) curves are for data from the first (second) subband. The red and blue dashed (nearly vertical) lines indicate expected LO phonon features calculated the same way as the red and blue arrows in (A) to (C), respectively (*17*). Curves are offset vertically for clarity, and the thin horizontal dashed-dotted line indicates zero for each curve.

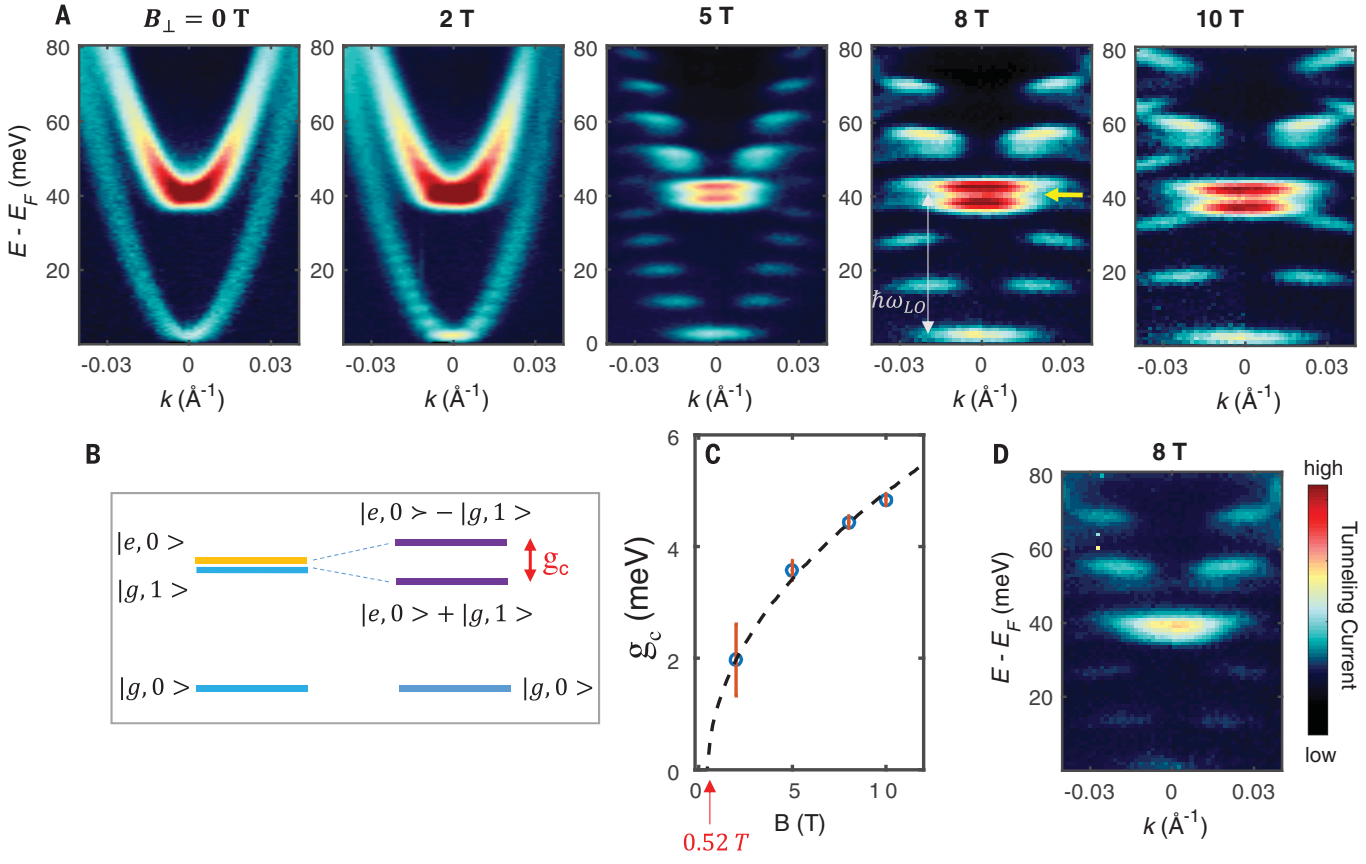

Fig. 3. Evolution of *E-k* spectra under perpendicular magnetic fields. (**A**) Measured spectra of the 2D electron system at a density of $n \sim 2.5 \times 10^{10}$ cm^{-2} for various perpendicularly applied magnetic fields. With increasing field, Landau quantizations with the cyclotron energy spacing $\hbar\omega_c$ become apparent. At $E - E_F \approx 40$ meV, the spectrum displays a level splitting in the 5-, 8-, and 10-T data. Tunneling into Landau levels (LLs) produces features resembling line segments. The features resulting from tunneling into a Landau index greater than zero appear as line segments at nonzero k that are slanted away from horizontal in the 5-, 8-, and 10-T data. The slants arise from the nonzero width of our square QWs. (**B**) A simple model that explains the level splitting. When the LO phonon energy matches the energy difference between the first (blue lines) and second (orange line) subband, a resonance occurs (purple lines) to produce the strongly coupled limit of an electron and a phonon—i.e., a polaron. The splitting arises because a long-lived composite state of the zeroth LL in the lowest (first) subband together with a LO phonon ($|g,1\rangle$) forms and resonantly interacts with the zeroth LL of the second subband ($|e,0\rangle$). (**C**) The splitting energies (blue circles) and error bars (vertical orange lines) are plotted as a function of magnetic field. The dashed line is a curve-fit of the four data points at nonzero B (from 2 to 10 T) to $g_c = a \times \sqrt{B - B_0}$ with fixed B_0 = 0.52 T, giving the fit parameter $a = 1.612$ meV$/\sqrt{(T)}$. (**D**) The splitting diminishes greatly for a spectrum measured at higher density, $n \sim 1.3 \times 10^{11}$ cm^{-2}, at 8 T. Color scales in (A) and (D) are calibrated so that the same currents give rise to the same colors and intensities (see also fig. S9).

bosonic mode. AlAs-like phonons exist at ~49 meV in $Al_{0.8}Ga_{0.2}As$, with an e-ph coupling constant larger than that of GaAs (*25*). This emergence of the kink coincides with an abrupt decrease in compressibility in a separate measurement (fig. S2). As localization arises in this regime, the onset of this feature may indicate the development of strongly bound states composed of a localized electron and a phonon—i.e., polarons (*26*). This idea is supported by the observation that the kink structure disappears above temperature $T \approx 16$ K (fig. S8), suggesting that the confinement from the disorder potential disappears by thermally activated electron hoppings.

To further investigate the effect of electron confinement, we applied perpendicular magnetic fields. As the magnetic field strength increases, the Landau quantization strongly modifies the dispersion into discrete Landau levels (LLs) (Fig. 3A). Because electrons are confined in a length scale of the magnetic length l_b, the dispersion spreads over a finite extent in the momentum direction whose magnitude is proportional to $1/l_b$.

At $B_\perp > 0.52$ T, all the electrons in the target QW fall into the lowest LL ($\nu < 2$). Near 36 meV ($\sim \hbar\omega_{LO}$, the energy of a LO phonon) above the bottom of the unoccupied bands, the spectrum shows an unexpectedly clear level splitting (yellow arrow). We explain this as the polaronic effect enhanced to the point where the LL of the second subband resonantly interacts with the LL of the first subband via a LO phonon. This is the signature behavior of the vacuum Rabi splitting—in this case, a "strong coupling" state between the zero-phonon and one-phonon states (*27*, *28*) (Fig. 3B)—and cannot be explained by any inelastic process involving simple phonon scatterings. Upon increasing the density of the 2D system so that only a few empty states (N_{empty}) remain available in the ground LL, the splitting disappears (Fig. 3D and fig. S9), consistent with the Rabi splitting picture. The splitting magnitude varies as $g_c \propto \sqrt{N_{empty}} \propto \sqrt{B - B_0}$ (Fig. 3C). Here, B_0 = 0.52 T is the field value at which electrons fully occupy the lowest LL and is roughly consistent with the density $n \sim 2.5 \times 10^{10}$ cm^{-2} determined by capacitance measurements. In this picture, the nearly dispersionless modes of LO phonons and the massive degeneracy of electrons, created by the flattening of the electronic dispersion in a perpendicular magnetic field, contribute to the formation of the strong coupling state. As we tune perpendicular magnetic fields, the electronic spectral function shows the transition from the weak limit (the self-energy treatment at B = 0) to the strong limit of e-ph interaction. We anticipate even stronger polaronic effects in other semiconductor systems,

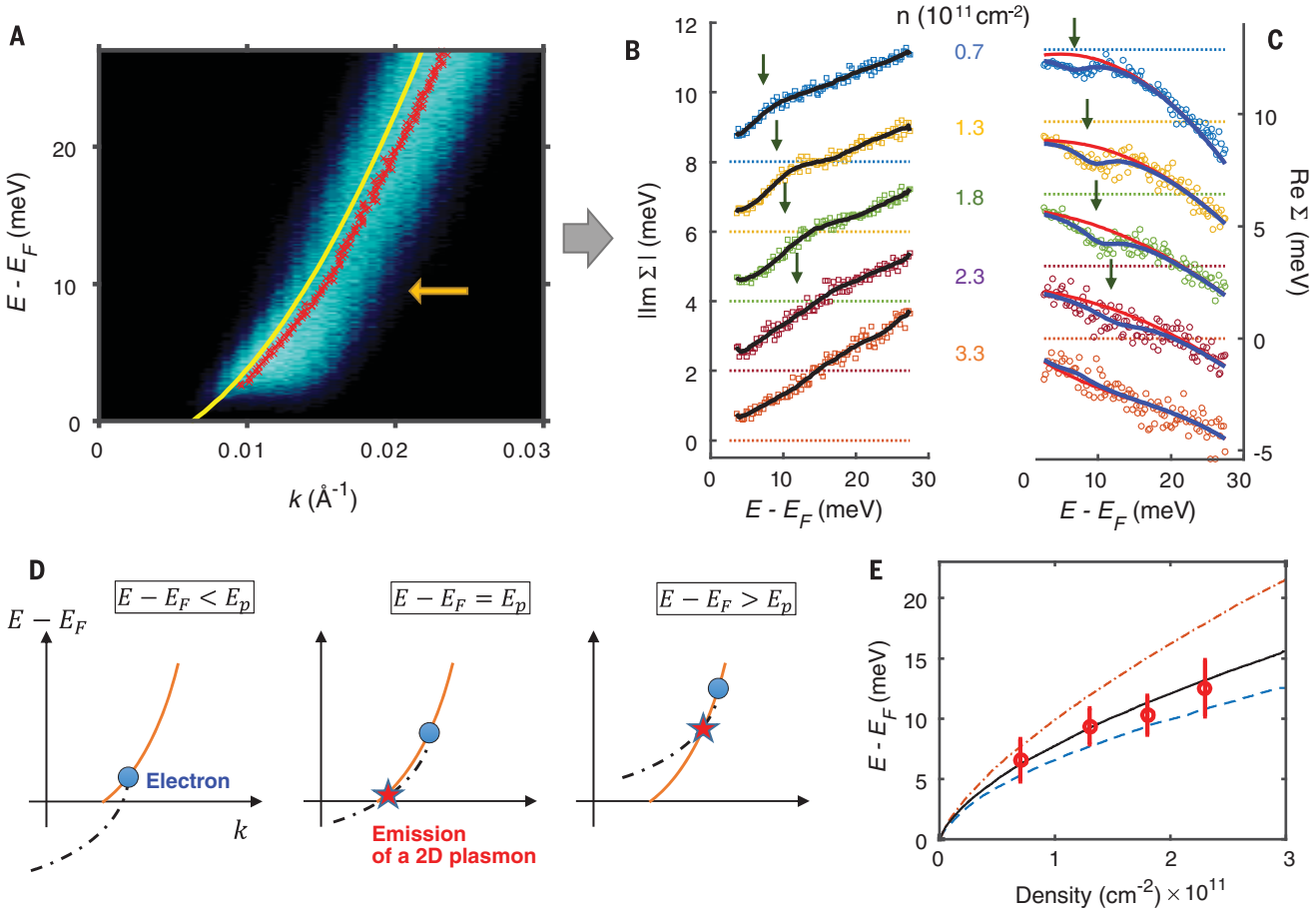

Fig. 4. Electron-electron interaction and plasmon scattering. (**A**) A zoom-in of the MERTS spectrum of the yellow rectangle in Fig. 2E measured at 3 K. The yellow curve shows the expected bare band dispersion, and red dots are measured peaks from fits to the data. There is a subtle, but statistically significant, kink in the red data points, indicated by the yellow arrow. (**B** and **C**) *Im*Σ and *Re*Σ from the spectra at various densities, indicated in the center. In (C), the red curves represent a slowly varying background signal obtained by curve-fitting the data away from the kink structure to a third-order polynomial, and the blue curves are curve-fits to the data with an additional Lorentzian term. The arrows in (C) point to the center of this Lorentzian. The same arrow locations are reproduced in (B), denoting a corresponding broad step feature in *Im*Σ. Black curves in (B) are simple moving averages to guide the eye. The thin horizontal dotted line indicates zero for each curve. (**D**) Electron-plasmon interaction. The orange curves represent electron dispersion, and dashed-dotted curves visualize final electron states in the event of emitting a plasmon. There exists a threshold energy E_p above which an injected electron (blue circles) can lose energy by scattering a plasmon and decay to lower-energy states that exist above E_F (red stars). (**E**) The locations of the features in (B) and (C) and how they change as a function of density. The red circles and error bars indicate peaks and widths of the Lorentzian function used to fit the data in (C). Also plotted are theoretically expected curves following (*33*). The blue dashed curve is from a semiclassical calculation, the red dashed-dotted curve is from a random phase approximation (RPA), and the black solid curve is for a RPA that accounts for the nonzero well width.

such as hole-doped GaAs, CdTe, and $SrTiO_3$, that have stronger e-ph interactions.

Theory predicts that e-e interactions lead to changes in thermodynamic quantities (*2*, *29*), but these effects are subtle, and the measurements are difficult to interpret (*30*). MERTS provides a direct means for observing these interactions in high-resolution spectra near the Fermi energy, where LO phonons have small impact and the dominant modifications to the spectra arise from e-e interactions (Fig. 4). At all densities, the measured $|Im\Sigma|$ reaches the minimum value near the Fermi level (Fig. 4B), in accord with the phase space restriction argument of Fermi liquid theory; the contribution from e-e interactions to the inverse of the quasiparticle lifetime, $1/\tau_q$ (or $2|Im\Sigma|$), decreases to zero quadratically in energy near the Fermi level (*31*). Owing to disorder, however, the inverse lifetime has a nonzero value even at E_F (*32*).

At low energies, additional structures can be seen in Fig. 4, B and C, that strongly depend on density (vertical arrows) and whose qualitative evolution as a function of density suggests that they originate from e-e interactions. The step-like features in *Im*Σ and dips in *Re*Σ can be explained as electrons being scattered by plasmons. The strength and locations of such features that vary as a function of electron density n is in quantitative agreement with the theory of plasmons in 2D (*5*, *6*, *33*). In this picture, the density dependence comes from a combination of a varying strength of the Coulomb screening by neighboring mobile electrons and a change of plasmon dispersion itself (fig. S6). The plasmons modify the electron dispersion near the Fermi level; their energy has a square-root density dependence, which is intrinsic to 2D plasmons (Fig. 4E). Our data constitute a direct measurement of quantities that were only theoretically investigated previously (*5*, *6*), demonstrating that the e-e scattering is suppressed near the Fermi level until plasmons meaningfully contribute to scattering processes. Using ARPES, the effects of plasmon scattering have been observed in the electron spectral function of massless electrons in graphene (*34*), but the features in those data did not directly reveal the plasmon dispersion relation.

The high energy and momentum resolution of MERTS make it particularly suitable for investigation of subtle quantum many-body effects. There are a few examples where this technique has immediate impact; under high magnetic fields, the method can allow visualization of

anisotropic wave functions of strongly correlated phases in the quantum Hall regime and provide crystallography of stripe phases, bubble phases, and Wigner crystals (*35*). With further improvements in materials, we anticipate that MERTS may become more generally applicable to semiconducting structures (and oxides) grown by MBE, because these can be grown with high-precision tunnel barriers and quantum wells. Importantly, MERTS is compatible with many embedded structures [e.g., (*36*)] and the highest-quality heterostructures for fundamental research, opening an avenue for investigating the physics of interacting particles in previously challenging geometries.

REFERENCES AND NOTES

1. G. Mahan, *Many-Particle Physics* (Springer, 2000).
2. G. F. Giuliani, G. Vignale, *Quantum Theory of the Electron Liquid* (Cambridge Univ. Press, 2005).
3. J. Bardeen, L. N. Cooper, J. R. Schrieffer, *Phys. Rev.* **108**, 1175–1204 (1957).
4. D. C. Tsui, H. L. Stormer, A. C. Gossard, *Phys. Rev. Lett.* **48**, 1559–1562 (1982).
5. R. Jalabert, S. Das Sarma, *Phys. Rev. B* **40**, 9723–9737 (1989).
6. P. Hawrylak, J. F. Young, P. Brockmann, *Semicond. Sci. Technol.* **9**, 432–435 (1994).
7. A. Damascelli, Z. Hussain, Z.-X. Shen, *Rev. Mod. Phys.* **75**, 473–541 (2003).
8. J. E. Hoffman *et al*., *Science* **297**, 1148–1151 (2002).
9. E. L. Wolf, *Principles of Electron Tunneling Spectroscopy* (Oxford Univ. Press, 2011).
10. J. A. Lebens, R. H. Silsbee, S. L. Wright, *Phys. Rev. B* **37**, 10308–10311 (1988).
11. R. K. Hayden *et al*., *Phys. Rev. Lett.* **66**, 1749–1752 (1991).
12. B. R. Snell *et al*., *Phys. Rev. Lett.* **59**, 2806–2809 (1987).
13. J. P. Eisenstein, T. J. Gramila, L. N. Pfeiffer, K. W. West, *Phys. Rev. B* **44**, 6511–6514 (1991).
14. E. E. Vdovin *et al*., *Science* **290**, 122–124 (2000).
15. A. Patanè *et al*., *Phys. Rev. B* **65**, 165308 (2002).
16. O. E. Dial, R. C. Ashoori, L. N. Pfeiffer, K. W. West, *Nature* **448**, 176–179 (2007).
17. Materials and methods are available as supplementary materials.
18. R. Winkler, *Spin-Orbit Coupling Effects in Two-Dimensional Electron and Hole Systems*, vol. 191 of *Springer Tracts in Modern Physics* (Springer, 2003).
19. J. M. Rowell, W. L. McMillan, W. L. Feldmann, *Phys. Rev.* **180**, 658–668 (1969).
20. H. Frohlich, *Proc. R. Soc. A Math. Phys. Eng. Sci.* **215**, 291–298 (1952).
21. T. Valla *et al*., *Science* **285**, 2110–2113 (1999).
22. C.-H. Park, F. Giustino, M. L. Cohen, S. G. Louie, *Phys. Rev. Lett.* **99**, 086804 (2007).
23. G. Grimvall, *Phys. Scr.* **14**, 63–78 (1976).
24. E. Z. Kuchinskii, I. A. Nekrasov, M. V. Sadovskii, *Phys. Rev. B* **80**, 115124 (2009).
25. S. Adachi, *J. Appl. Phys.* **58**, R1–R29 (1985).
26. M. H. Degani, G. A. Farias, *Phys. Rev. B* **42**, 11950–11952 (1990).
27. T. Inoshita, H. Sakaki, *Phys. Rev. B* **56**, R4355–R4358 (1997).
28. G. Scalari *et al*., *Science* **335**, 1323–1326 (2012).
29. R. Asgari *et al*., *Phys. Rev. B* **71**, 045323 (2005).
30. Y.-W. Tan *et al*., *Phys. Rev. Lett.* **94**, 016405 (2005).
31. G. F. Giuliani, J. J. Quinn, *Phys. Rev. B* **26**, 4421–4428 (1982).
32. S. Q. Murphy, J. P. Eisenstein, L. N. Pfeiffer, K. W. West, *Phys. Rev. B* **52**, 14825–14828 (1995).
33. E. H. Hwang, S. Das Sarma, *Phys. Rev. B* **64**, 165409 (2001).
34. A. Bostwick, T. Ohta, T. Seyller, K. Horn, E. Rotenberg, *Nat. Phys.* **3**, 36–40 (2007).
35. J. Jang, B. M. Hunt, L. N. Pfeiffer, K. W. West, R. C. Ashoori, *Nat. Phys.* **13**, 340–344 (2017).
36. A. Singha *et al*., *Science* **332**, 1176–1179 (2011).

ACKNOWLEDGMENTS

We thank P. A. Lee, B. Skinner, J. G. Checkelsky, and L. Levitov for helpful discussions. The work at MIT was funded by the Basic Energy Sciences Program of the Office of Science of the U.S. Department of Energy through contract no. FG02-08ER46514 and by the Gordon and Betty Moore Foundation through grant GBMF2931. The work at Princeton University was funded by the Gordon and Betty Moore Foundation through the EPiQS (Emergent Phenomena in Quantum Systems) initiative grant GBMF4420 and by the National Science Foundation MRSEC (Materials Research Science and Engineering Centers) grant DMR-1420541. The data that support the findings of this study are available from the corresponding authors on request.

SUPPLEMENTARY MATERIALS

www.sciencemag.org/content/358/6365/901/suppl/DC1
Materials and Methods
Supplementary Text
Figs. S1 to S9
References (*37*–*40*)

4 January 2017; accepted 5 October 2017
10.1126/science.aam7073

Full momentum- and energy-resolved spectral function of a 2D electronic system

Joonho Jang, Heun Mo Yoo, L. N. Pfeiffer, K. W. West, K. W. Baldwin and Raymond C. Ashoori

Science **358** (6365), 901-906.
DOI: 10.1126/science.aam7073

Delving deep into electronic properties

The spectral function of a material, which reflects the distribution of its electronic states as a function of momentum and energy, carries a wealth of information on its properties. However, measuring the spectral function directly is tricky, particularly in systems inaccessible to surface probes or in insulators. Jang *et al.* introduce a method dubbed momentum- and energy-resolved tunneling spectroscopy, in which electrons tunnel from a probe layer to unoccupied states in a target layer deep in a heterostructure. Because the momentum and energy of the electrons are tightly controlled, the measured tunneling probability is proportional to the spectral function of the target system.

Science, this issue p. 901